

Research article

Mohsen Heidari*, Vahid Faramarzi, Zohreh Sharifi, Mahdiah Hashemi, Shahram Bahadori-Haghighi, Babak Janjan and Derek Abbott

A high-performance TE modulator/TM-pass polarizer using selective mode shaping in a VO₂-based side-polished fiber

<https://doi.org/10.1515/nanoph-2021-0225>

Received May 9, 2021; accepted August 4, 2021;

published online August 18, 2021

Abstract: The reversible insulating-to-conducting phase transition (ICPT) of vanadium dioxide (VO₂) makes it a versatile candidate for the implementation of integrated optical devices. In this paper, a bi-functional in-line optical device based on a four-layer stack of PMMA/graphene/VO₂/graphene deposited on a side-polished fiber (SPF) is proposed. The structure can be employed as an ultra-compact TE modulator or a TM-pass polarizer, operating at 1.55 μm . We show that the ICPT characteristic can be used for polarization-selective mode shaping (PSMS) to manipulate orthogonal modes separately. On the one hand, as an optical modulator, the PSMS is used to modify mode profiles so that the TE mode attenuation is maximized in the off-state (and IL is minimized in the on-state), while the power carried by the TM mode remains unchanged. As a result, a TE modulator with

an ultrahigh extinction ratio (ER) of about ER = 165 dB/mm and a very low insertion loss (IL) of IL = 2.3 dB/mm is achieved. On the other hand, the structure can act as a TM-pass polarizer featuring an extremely high polarization extinction ratio (PER) of about PER = 164 dB/mm and a low TM insertion of IL = 3.86 dB/mm. The three-dimensional heat transfer calculation for the ICPT process reveals that the response time of the modulator is in the order of few nanoseconds. Moreover, the required bias voltage of the proposed device is calculated to be as low as 1.1 V. The presented results are promising a key step towards the realization of an integrated high-performance in-line modulator/polarizer.

Keywords: graphene; modulator; polarizer; selective mode shaping; side-polished fiber; vanadium dioxide.

1 Introduction

Optical modulators are key components in many optical systems for manipulating the light passing through the device. In general, optical modulators modify the characteristics of light, such as its phase, amplitude, or polarization. In this regard, several types of optical modulators have been proposed and fabricated based on the electro-absorption (EA) [1], electro-optic (EO) [2], magneto-optic [3], and thermo-optic (TO) [4–6] effects. In fiber-optic telecommunication networks, a monolithic approach is preferred over the conventional approach that requires the interruption of the fiber by insertion of an external device [7]. The conventional approach suffers from several drawbacks including mechanical instability and high insertion loss. In contrast, in-line fiber platforms potentially resolve these issues because the devices can be embedded within the fiber in such a way that propagating the optical field evanescently interacts with the surrounding active media.

Fiber-based EA modulators utilize materials whose losses can be effectively modulated. Various materials,

*Corresponding author: **Mohsen Heidari**, Department of Electrical and Computer Engineering, Tarbiat Modares University, 14115-116 Tehran, Iran, E-mail: mh.heidari@modares.ac.ir. <https://orcid.org/0000-0002-5041-053X>

Vahid Faramarzi and Babak Janjan, Department of Electrical and Computer Engineering, Tarbiat Modares University, 14115-116 Tehran, Iran, E-mail: v.faramarzi@modares.ac.ir (V. Faramarzi), b.janjan@modares.ac.ir (B. Janjan)

Zohreh Sharifi, Department of Electrical and Computer Engineering, University of Victoria, Victoria, BC V8W 3P6, Canada, E-mail: zsharifi@uvic.ca

Mahdiah Hashemi, Department of Physics, College of Science, Fasa University, Fasa 74617-81189, Iran, E-mail: mahdiah.hashemi@gmail.com

Shahram Bahadori-Haghighi, School of Electrical and Computer Engineering, Shiraz University, Shiraz, 71348-51154 Iran, E-mail: sbahadori@shirazu.ac.ir

Derek Abbott, School of Electrical and Electronic Engineering, The University of Adelaide, Adelaide, SA 5005, Australia, E-mail: derek.abbott@adelaide.edu.au. <https://orcid.org/0000-0002-0945-2674>

including transparent conductive oxides (TCOs) [8, 9], optical phase change materials (O-PCM) [10, 11], and two-dimensional (2D) materials such as graphene [12], have already been employed to realize high-performance and compact EA modulators.

Note that O-PCMs show a reversible phase transition between an insulating phase (with low loss) and a conducting phase (with high loss), which leads to significant changes in their optical properties. This property of O-PCMs has been employed to realize various photonic devices [5]. Among them, vanadium dioxide (VO_2) has recently attracted significant attention due to its unique optical and thermal properties, which can be used in active photonic devices [13, 14]. Here, VO_2 exhibits a reversible abrupt insulating-to-conducting phase transition (ICPT) that can be originated by applying an electric field larger than the threshold field of $\sim 6.5 \times 10^7$ V/m [15] or by adjusting the temperature of VO_2 above $\sim 68^\circ\text{C}$ [10]. The reverse mechanism, the conducting-to-insulating phase transition (CIPT), occurs when the applied electric field to VO_2 is removed or the VO_2 is sufficiently cooled. The ICPT in VO_2 is accompanied by a considerable change in the refractive index so that the real part varies from 3.24 to 1.58 and the imaginary part varies from 0.353 to 2.63 at the wavelength of $\lambda = 1.55 \mu\text{m}$ [16, 17]. This significant change in the imaginary part of the refractive index (or equivalently in the VO_2 propagation loss) allows the design of EA modulators with small footprints [18, 19]. Moreover, owing to the considerable change in the real part of the VO_2 refractive index and also its unique thermal properties, it can be used in EO and TO modulators [10].

Although such devices are available in silicon photonic platforms, their high-performance in-line fiber counterparts have not widely been explored. Fiber optics can be easily covered by active materials such as VO_2 , TCOs and graphene [20]. However, as the light-matter interaction is weak, this platform requires larger optical configurations for coupling the propagating light to the active material. This is due to the spatial separation of the confined light in the fiber core from the coating material on the fiber cladding. To overcome this deficiency, the idea of side-polished fibers (SPF) has been introduced [21, 22]. In SPFs a portion of the fiber cladding is removed to bring the active material closer to the fiber core. This can significantly enhance the interaction of light evanescent field with an active material that reduces the size of the device [22, 23]. Several theoretical and experimental studies on the application of side-polished fibers have been reported including modulators [24], polarizers [25–27], filters [28], biosensors [29–31], and switches [21]. A variety of materials

such as polymers, polymethyl methacrylate (PMMA), high index polyvinyl butyral (PVB), and chalcogenide thin films have already been used as coating layers on SPFs in order to manipulate the mode profile and for functionalization in order to bind to biological analytes for sensing applications [21, 31–33]. In addition, several SPF-based polarizers and modulators are integrated with overlaid graphene, which benefits from its broadband tunability [24, 34, 35]. However, due to the 2D nature of graphene (with a thickness of 0.34 nm), the light-graphene interaction is poor [36], which limits the performance and compactness of such devices because extended lengths are required [37].

In EA, EO, and TO modulators based on O-PCMs and TCOs the tunability is obtained by applying an electric field or by heat generation using a metal electrode. Such metal electrodes can significantly increase the on-state insertion loss of the modulator. One potential approach for eliminating metal electrode losses in the on-state is to use graphene as the electrode to apply the required electric field across the active material overlay [34]. It should also be mentioned that due to the significant loss of VO_2 in the low-loss operating state (i.e. the insulating phase), it is still challenging to achieve modulators with low insertion loss and high extinction ratio. In this study, we propose an optical TE modulator/TM-pass polarizer comprising a stack of PMMA/graphene/ VO_2 /graphene on the top of an SPF to overcome the mentioned shortcomings. This structure selectively modulates the TE-polarized mode, while the power carried by the TM polarization remains unchanged. Moreover, this four-layer stack provides us with a polarization-selective mode shaping (PSMS) of the TE mode to extremely enhance the extinction ratio (ER) and minimize the insertion loss (IL) of the modulator.

According to the presented results, PSMS can provide an extremely higher ER of about 165 dB in comparison to state-of-the-art fabricated isolators with ERs in the order of about 10 dB [33, 35, 38]. Such an outstanding achievement is accompanied by a moderate IL of 2.3 dB. Moreover, it is estimated that the modulation speed of the proposed PSMS-based EA modulator is 125 MHz which is five orders of magnitude higher than that of the state-of-the-art EA modulators (< 300 Hz) [35].

The details of the PSMS mechanism for both the TE and TM modes are investigated in Section 2. The reshaping of the TE- and TM-polarized modes in response to the phase change of VO_2 is presented. In the next step in Section 3, the effects of the geometrical parameters, such as the height of the Polish fiber and the VO_2 thickness on the PSMS, are studied because they can effectively be engineered to achieve the highest performance. Then, the coupling losses

of the tapered entrance and exit sections are calculated and are taken into account in the total extinction ratio and insertion loss of the modulator and polarizer. Afterward, the modulation speed is also studied in Section 4 where two speed-limiting mechanisms are considered. First, the time delay due to the RC time constant of the device is calculated. Second, the heating and cooling time delays of the VO₂ layer are determined precisely based on the conductive and convective heat transfer calculations. Finally, a summary of the results and study is provided in Section 5.

2 Device structure and operating principle

The schematic of the proposed PSMS-SPF modulator/polarizer is illustrated in Figure 1. The device consists of a PMMA/graphene/VO₂/graphene stack grown on a side-polished standard single-mode fiber (Corning SMF-28) with a core/cladding diameter of 8.2/125 μm . The two graphene sheets are employed as the top and bottom electrodes to apply an external voltage across the VO₂ slab. As it is shown in Figure 1a, in order to minimize the coupling loss, tapers are used for gradual transitions from the unpolished fiber to the uniform D-shaped region, and vice versa. The cross-sectional view of the proposed PSMS-SPF modulator/polarizer is shown in Figure 1b. The parameters w and d represent the width and thickness of the VO₂ layer, respectively. The polished height (the distance between the core center and the polished surface) is also denoted by h . The side polishing allows access to the propagating light within the core without breaking the fiber path. The

proposed PSMS-SPF device has two operating modes, i.e. TM-pass polarizer and TE modulator that are schematically shown in Figure 1c and d, respectively.

In conventional VO₂-based EA modulators, the phase state of VO₂ (the propagation loss of VO₂) controls the transmission of light through the modulator. In other words, the low-loss insulating and high-loss conducting phases of VO₂ with the corresponding refractive indices of $n = 3.243 + 0.353i$ and $1.58 + 2.63i$ result in on- and off-states of the EA modulator, respectively. In contrast, our proposed design with PSMS-SPF configuration utilizes the variation of the real part of the refractive index to selectively manipulate the TE-mode profile.

In order to understand the concept behind it, the electric field profile of the TE (TM) mode in the bare SPF is shown in Figure 2a (Figure 2d). On the other side, the electric field profiles of the TE (TM) mode of the proposed PSMS-SPF with PMMA/graphene/VO₂/graphene stack coating in the insulating and conducting phases of VO₂ are respectively shown in Figure 2b and c (Figure 2e and f). The geometrical parameters are taken as $w = 10 \mu\text{m}$, $d = 10.8 \text{ nm}$, and a PMMA thickness of 600 nm. As it can be seen in Figure 2, the TE mode profile is highly affected by the coatings and especially the phase change of the VO₂, while the TM mode exhibits little sensitivity. In order to gain a better insight into the TE (TM) field profile variations, the electric field amplitudes along the central white dashed lines of Figure 2b and c (Figure 2e and f), are illustrated in Figure 2g. It is obvious that when VO₂ is in the low-loss insulating phase, the TE mode moves toward it so that high light-VO₂ interaction is obtained. As a result, the attenuation of optical power is enhanced and the modulator is set at the off-state although the intrinsic loss of VO₂ is low. On the other hand, when the VO₂ is in the conducting phase, the TE mode gets away from the lossy VO₂, which results in minimal insertion loss and consequently on-state of the modulator. Therefore, it can be said that PSMS significantly enhances the overlap of the optical mode with VO₂. Figure 2g qualitatively shows how much the TE and TM modes move toward or away from the VO₂ layer in different states (for more details, see Supplement 1, Section I).

To physically explain the TE mode-resaping, it is worth noting that light generally moves toward layers with high refractive indices and this leads to the mode profile reshaping. Although this mode reshaping can occur for both TE and TM modes, it is possible to design appropriate coating layers to achieve selective-mode profile reshaping of either TE or TM mode. The mechanism of PSMS in our proposed stack of coating layers is schematically illustrated in Figure 3. As it is known, the dominant electric

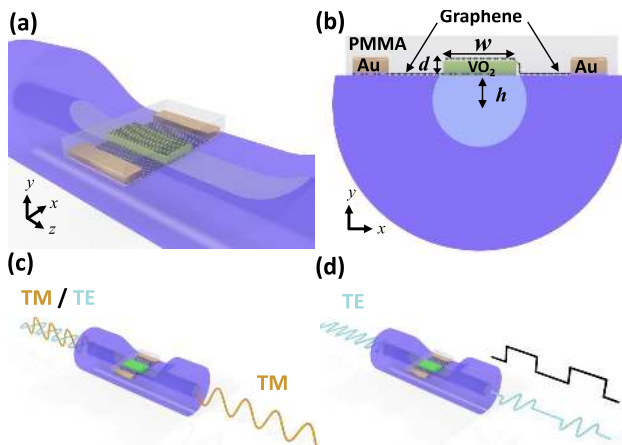


Figure 1: (a) The perspective view of the proposed in-line fiber modulator formed by overlaying a VO₂ layer on the side-polished fiber. (b) The cross-section details. Bi-function operation as (c) TM-pass polarizer and (d) TE modulator.

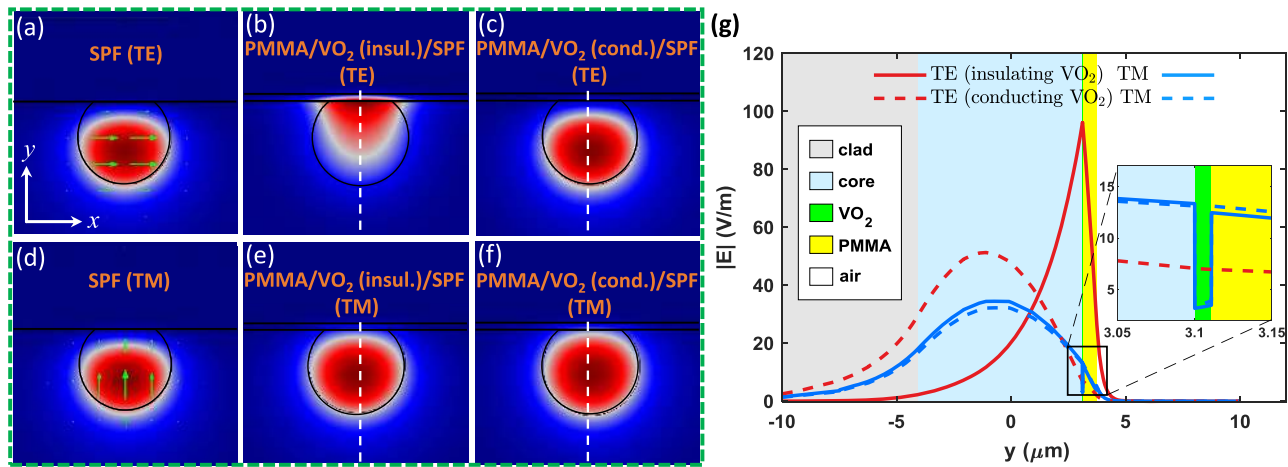


Figure 2: The electric field profiles of (a) TE mode and (d) TM mode of the bare SPF. The electric field profile of (b) TE mode and (f) TM mode in the PSMS-SPF with PMMA/graphene/VO₂/graphene coatings where VO₂ is in the insulating phase. The electric field profile of (c) TE mode and (e) TM mode of the PSMS-SPF where VO₂ is in the conducting phase. The green arrows in (a) and (d) illustrate the magnitude and direction of the electric field. (g) The electric field amplitude of TE and TM modes along the central cut-lines (white dashed lines) of (b), (c), (e) and (f).

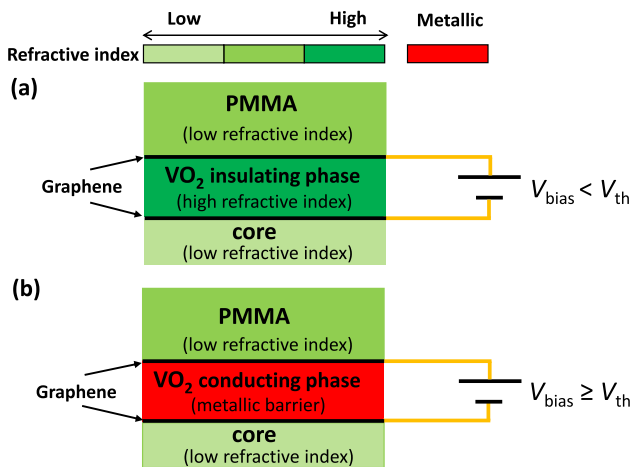


Figure 3: The schematic view of PSMS mechanism for TE mode, (a) in the insulating phase and (b) in the conducting phase.

field component of the TE mode lies along the x -direction (see green arrows in Figure 2a). Due to the continuity of the tangential components of the electric fields (E_x), it is expected that the TE mode profile must be continuous in the three-layer stack of PMMA/VO₂/core shown in Figure 3. Now as can be seen in Figure 3a, when the bias voltage V_{bias} of the device applied to the graphene sheets is set to zero or when it is below the threshold voltage, the VO₂ is in the insulating phase with a refractive index of $n = 3.243 + 0.353i$. In this case, the structure of modulator can be considered as an LHL (L = low refractive index, H = high refractive index) stack in which the VO₂ layer with $n_{\text{VO}_2} = \text{Re}(n) = 3.243$ is sandwiched between the fiber core (with the low refractive index of $n_{\text{core}} = 1.4682$)

and the PMMA coating (with the low refractive index of $n_{\text{PMMA}} = 1.49$). Therefore, the high refractive index of VO₂ pulls the TE profile upward and it can act as an optical connection between the fiber core and the thick PMMA coating due to the continuity of the TE mode (see Figure 2b and the red line in Figure 2g). As a result, the propagating TE mode undergoes high attenuation because of the high overlap between the field profile and the insulating VO₂ that yields the off-state of the modulator. It should be emphasized that although graphene electrodes can also cause losses at $\lambda = 1.55 \mu\text{m}$ when their chemical potentials μ_c are less than 0.4 eV, the loss of VO₂ is the only mechanism that contributes to the attenuation of the TE mode because the chemical potentials are assumed to be 0.75 eV. Therefore, graphene electrodes can be considered almost lossless (see Supplement 1, Section II and Figure S3).

In the case of TM polarized light with its dominant electric field perpendicular to the interfaces (see Figure 2d, the continuity condition of the perpendicular component of the displacement field $D_{1,y} = D_{2,y}$ (i.e. $n_1^2 E_{1,y} = n_2^2 E_{2,y}$) leads to reduced penetration of the electric field into the VO₂ layer with its high real part of the refractive index. Thus, the optical connection cannot be established between the guided TM-mode inside the fiber core and the PMMA overlaid. As a result, the TM mode profile remains unchanged (see Figure 2e and the blue line in Figure 2g). According to the inset of Figure 2g and as it is expected, lower amplitudes of the electric field inside the VO₂ in the TM polarization compared to that of the TE mode is apparent.

As can be seen in Figure 3b, when the bias voltage exceeds V_{th} , the VO₂ phase changes from the insulating

to conduction one, which results in a significant reduction in the real part of its refractive index from 3.243 to 1.58. In addition, the sign of the real part of VO_2 permittivity, $\epsilon_{\text{VO}_2} = n_{\text{VO}_2}^2$ changes from a positive (+10.3924) to a negative value (−4.4205) that indicates the transition from a dielectric to metal leading to the formation of an LML stack (L = low refractive index, M = metal). Keeping in mind the field isolated nature of metals, the electromagnetic boundary conditions imply $E_x \approx 0$ and $E_y \approx 0$ at the conducting VO_2 interfaces with both the PMMA and fiber core [39]. This causes discontinuities in the electric field profiles of both the TE and TM modes and as a result, no optical connection can be established between the thick PMMA and the fiber core. Therefore, as it is shown in Figure 2c and f, there is no significant change in the profiles of the TE/TM modes. In this case, as it is confirmed by the blue and red dashed lines in Figure 2g, light is trapped at the bottom of the fiber core and is separated from the lossy VO_2 so that the insertion loss is reduced and the modulator is set to the on-state. Moreover, for the case of bare SPF as it is shown Figure 2a and d, the profile of both the TE and TM modes are pushed down to the bottom of the core. This is due to the higher refractive index of silica cladding ($n_{\text{clad}} = 1.4615$) at the bottom compared to that of the air cladding ($n_{\text{air}} = 1$) at the top polished interface.

3 Results and discussion

3.1 TM-pass polarizer

To elaborate further on the characteristics of the TE modulator/TM-pass polarizer, we have investigated the device response to variations of the parameters such as VO_2 thickness, d and the polished height, h . The most important characteristics of each modulator/polarizer are the extinction ratio (ER) and insertion loss (IL). To achieve the desired extinction ratio and low insertion loss, the parameters of the device such as the polished height and the VO_2 thickness should be engineered. Figure 4a shows the variation of $\text{IL}_{\text{off}}^{\text{TE/TM}}$ and $\text{IL}_{\text{on}}^{\text{TE/TM}}$ and Figure 4b shows the off-state effective mode indices variation of both TE and TM modes as a function of VO_2 thickness. In order for the PSMS-SPF to operate as a TE modulator, the propagation loss of the device should be modulated between the minimum and maximum losses. Thus, the state of the device should be changed between on- and off-states.

It is interesting to note that this device can be used as an extremely high-performance polarizer. As shown in Figure 4a, to find the optimum thickness of the VO_2 layer

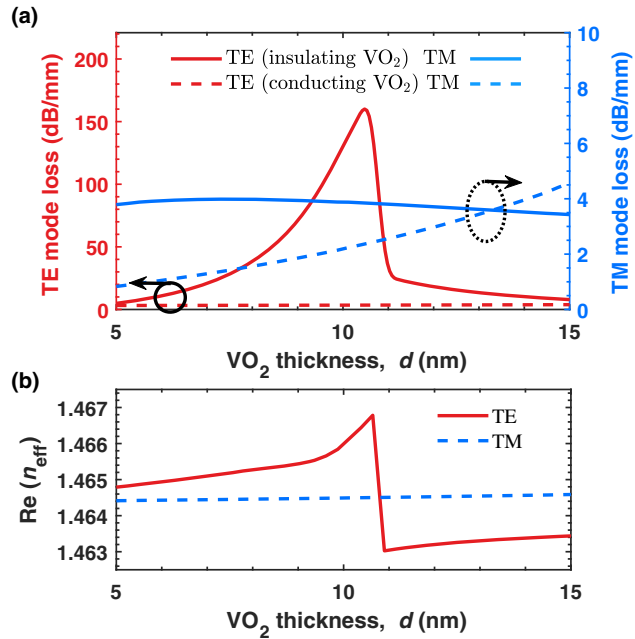


Figure 4: (a) The propagation losses of the TE and TM modes as a function of the VO_2 thickness in both insulating and conducting phases. At $d = 10.8$ nm, the device can be employed as the TM-pass polarizer. (b) The calculated changes in the real part of TE and TM mode indices versus the thickness of VO_2 .

in which the extinction ratio of the device is maximized, its thickness is swept from 5 to 15 nm, and the insertion loss of both TE and TM modes are calculated for both insulating and conducting phases of the VO_2 layer. Here, a constant polished height of $h = 3.1 \mu\text{m}$ is considered. It can be seen that the off-state insertion loss of the TE mode, $\text{IL}_{\text{off}}^{\text{TE}}$ reaches its maximum value of 168 dB/mm at $d = 10.8$ nm. On the other hand, in the case of TM mode, it can be seen that both off-state and on-state insertion losses, $\text{IL}_{\text{off}}^{\text{TM}}$ and $\text{IL}_{\text{on}}^{\text{TM}}$ have minor sensitivity to the changes in the VO_2 thickness and have low and almost constant values of about 4 dB/mm. This high off-state insertion loss of the TE mode, $\text{IL}_{\text{off}}^{\text{TE}}$ (near $d = 10.8$ nm) and the very low off-state insertion loss of the TM mode, $\text{IL}_{\text{off}}^{\text{TM}}$ evokes the function of TM-pass polarizer. Therefore, to operate as a TM-pass polarizer, the device should always be in the off-state that the highest TE mode damping occurs. The polarization extinction ratio (PER) is defined as the ratio of the power carried by the TM mode to the power carried by the TE mode, represented in dB as $\text{PER}^{\text{Polarizer}} = \text{IL}_{\text{off}}^{\text{TE}} - \text{IL}_{\text{off}}^{\text{TM}}$, is ~ 164.14 dB. Also, the insertion loss of the TM-pass polarizer equals to the off-state insertion loss of the TM mode as $\text{IL}^{\text{Polarizer}} = \text{IL}_{\text{off}}^{\text{TM}}$, that is ~ 3.86 dB.

Figure 4b shows the effective index variation of the guided TE (red line) and TM (blue dashed line) modes

as functions of the VO₂ thickness in the insulating phase (off-state). As can be seen, as d increases, the effective mode index of the TE mode also increases and reaches its maximum value at $d = 10.8$ nm and then decreases rapidly. This means that the TE mode profile is pulled up to the medium (PMMA/VO₂ stack) with a higher effective refractive index. With further increase in d , the 600 nm-thick PMMA/ d nm-thick VO₂ stack provides a much higher effective refractive index than the refractive index of core, which leads to a decoupling between the core guided mode and the upper coatings. Thus, the TE mode profile is pushed down again. In contrast to the TE mode, the effective mode index of the TM mode is slightly sensitive to the changes in VO₂ thickness and is almost constant.

It should be noted that VO₂ material has already been deposited on graphene [4, 40], which shows that our proposed structure is experimentally feasible. However, the most challenging part of realizing such a VO₂-based stack on an SPF is to deposit an ultrathin VO₂ layer (below 10 nm) on the graphene sheet. Recently, the techniques of Ar-ion milling [41], pulsed laser deposition (PLD) [42, 43], and a readily implemented synthesis method are managed to achieve ultrathin VO₂ layers with thicknesses lower than 4 nm [41], 5 nm [42], 2 nm [43], and 10 nm [44]. In our proposed device, the best performance is achieved at the VO₂ thickness of ~ 10.8 nm.

3.2 TE modulator

The extinction ratio of the TE polarizer can be defined as the difference between the TE mode insertion losses of the device in the off-state and the on-state as $ER^{\text{Modulator}} = IL_{\text{off}}^{\text{TE}} - IL_{\text{on}}^{\text{TE}}$. Also, the modulator insertion loss equals the on-state insertion loss of TE mode, as $IL^{\text{Modulator}} = IL_{\text{on}}^{\text{TE}}$. As mentioned before in Section 2, the TE mode response of the device has a considerable sensitivity to the changes in both geometrical parameters and the phase state of the VO₂ layer. In the above calculations and results shown in Figure 4a and b, a constant polished height of $h = 3.1$ μm is considered. In order to clearly show the influence of the polished height variation on the performance of the proposed modulator, both off- and on-states insertion losses, and extinction ratio are calculated as a function of the polished height (at constant $d = 10.8$ nm) and depicted in Figure 5a. For a better representation of the amount of intersection of the polished surface with the core/clad area, the residual radius is defined as $RR = h - r$, where r denotes the core radius. A negative RR indicates that the polished surface enters the core and a positive RR indicates that the polished surface lies in the cladding, and an $RR = 0$ indicates that the polished surface is at the

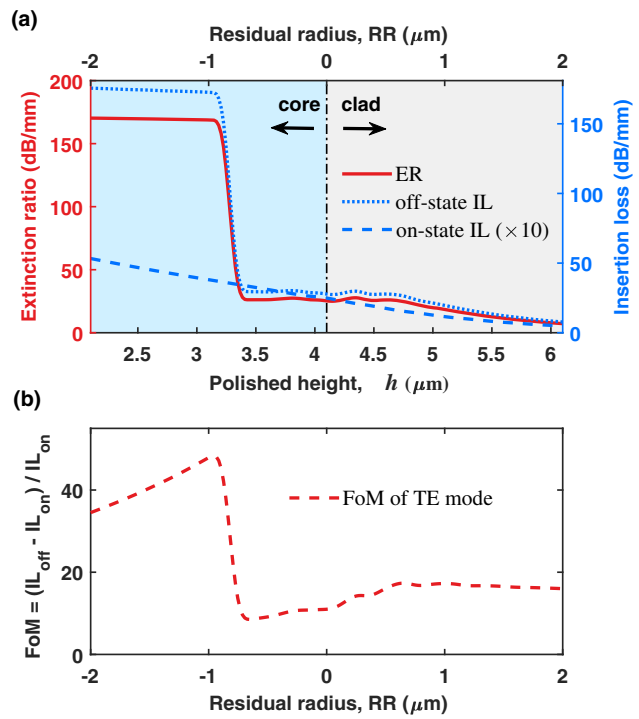


Figure 5: (a) The extinction ratio and insertion loss (i.e. the on-state IL) of the TE modulator as a function of both polished height and residual radius. (b) FoM of the TE modulator versus the residual radius.

core/clad interface. As it is seen in Figure 5a, the on-state insertion loss (blue dashed line) increases uniformly with decreasing RR , because the interaction between the VO₂ layer and the evanescent field of TE mode has got stronger. Also, similar behavior is observed for the off-state insertion loss (blue dotted line), which increases with decreasing RR . Besides, a very sharp increase occurs near $RR = -1$ μm (or equivalently $h = 3.1$ μm), and then, with a further decrease in the residual radius, the off-state insertion loss increases slightly. The reason is that for $RR \leq 1$ μm , the TE mode profile has tightly drawn to the mentioned four-layer stack due to its higher refractive index and the VO₂ (insulating phase) leads to an attenuation of the power carried by the TE mode.

Similar to the off-state insertion loss, the extinction ratio (red line) of the modulator for the TE mode increases rapidly from 32 dB/mm to 165 dB/mm at $RR = -1$ μm . With a further decrease in RR , the extinction ratio remains constant. It may be concluded that an $RR < -1$ μm is sufficient to achieve a high performance and high extinction ratio modulator; however, this conclusion is not always correct. Although for $RR \leq -1$ μm , the extinction ratio reaches its maximum (~ 165 dB/mm) and remains constant. However, the on-state insertion loss increases as the residual

radius decreases leading to an increase in the optical power attenuation of the TE mode in the on-state (i.e. on-state insertion loss). The performance of modulators is related to both the high extinction ratio and low on-state insertion loss. To show the impact of the residual radius on the performance of modulators, a figure of merit (FoM) is defined as $\text{FoM} = (\text{IL}_{\text{off}} - \text{IL}_{\text{on}}) / \text{IL}_{\text{on}}$, as shown in Figure 5b. As can be seen, the FoM at $\text{RR} \approx -1 \mu\text{m}$ reaches a maximum of about 49, in which the highest modulator performance with the highest extinction ratio and the optimum amount of the on-state insertion loss are achieved simultaneously.

3.3 Coupling losses

It should be noted that at all the results discussed in the previous section, the coupling loss of TE/TM mode in the transitional polished tapers at the beginning and the end of the SPF are not considered. Profiles of TE and TM modes at three points, (I) before the entrance transition section, (II) in the entrance transition section, and (III) in the active region of the device for on- and off-states are shown in Figure 6a. As can be seen, both TE and TM mode shapes change from a symmetric circular shape to a D-shape. In addition, the TE mode is more affected by the fiber shape deformation and the VO_2 phase-change, so undergoes greater coupling loss than the TM mode. As light propagates through the exit transition section, a reverse mode deformation occurs from the D-shape to the symmetric one.

Here, to account for these coupling losses, a 3D-FDTD method is used with the assumption of a typical transition length of $L_{\text{tr}} = 4 \text{ mm}$ [45]. The calculated coupling losses of the device in the on- and off-states for the TE and TM modes are $\alpha_{\text{on}}^{\text{TE}} = 0.24 \text{ dB}$, $\alpha_{\text{on}}^{\text{TM}} = 0.15 \text{ dB}$, $\alpha_{\text{off}}^{\text{TE}} = 0.37 \text{ dB}$, and $\alpha_{\text{off}}^{\text{TM}} = 0.18 \text{ dB}$, respectively. Therefore, by inclusion of coupling losses, the total extinction ratio and total insertion loss of the proposed modulator/polarizer with the active region length of L_{act} can be obtained as:

$$\text{ER}_{\text{Total}}^{\text{Modulator}} = (\text{IL}_{\text{off}}^{\text{TE}} - \text{IL}_{\text{on}}^{\text{TE}}) \times L_{\text{act}} + 2(\alpha_{\text{off}}^{\text{TE}} - \alpha_{\text{on}}^{\text{TE}}) \quad (1)$$

$$\text{IL}_{\text{Total}}^{\text{Modulator}} = \text{IL}_{\text{on}}^{\text{TE}} \times L_{\text{act}} + 2\alpha_{\text{on}}^{\text{TE}}$$

$$\text{PER}_{\text{Total}}^{\text{Polarizer}} = (\text{IL}_{\text{off}}^{\text{TE}} - \text{IL}_{\text{off}}^{\text{TM}}) \times L_{\text{act}} + 2(\alpha_{\text{off}}^{\text{TE}} - \alpha_{\text{off}}^{\text{TM}}) \quad (2)$$

$$\text{IL}_{\text{Total}}^{\text{Polarizer}} = \text{IL}_{\text{off}}^{\text{TM}} \times L_{\text{act}} + 2\alpha_{\text{off}}^{\text{TM}}$$

Assuming $L_{\text{act}} = 1 \text{ mm}$, the results show that the minimum total extinction ratio and insertion loss of modulator are as high as $\text{ER}_{\text{Total}}^{\text{Modulator}} = 165 \text{ dB/mm}$, and

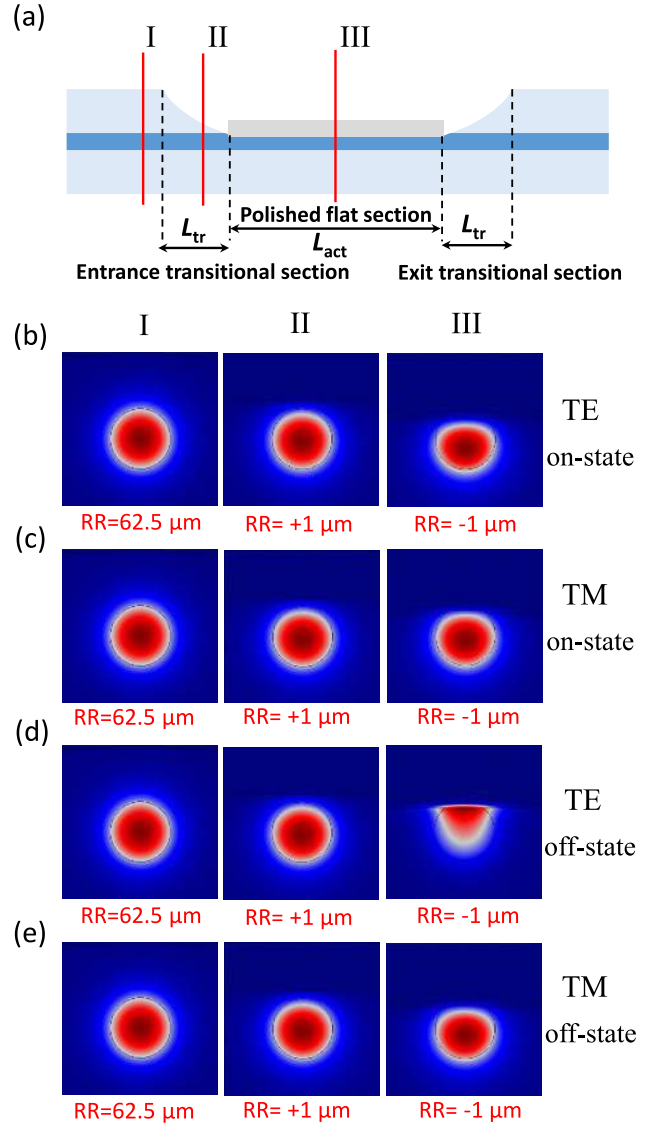


Figure 6: (a) The schematic side view of the SPMS-based SPF. (b) TE mode profiles of the on-state at three different points at (I) entrance tapered region, (II) center of the polished flat region, and (III) exit tapered region. (c) TM mode profiles of the on-state, (d) TE mode profiles of the off-state, and (e) TM mode profiles of the off-state at three different points. The red values below each graphs shows the residual radius of the structure at each point.

$\text{IL}_{\text{Total}}^{\text{Modulator}} = 2.3 \text{ dB/mm}$, respectively. Also, in the case of TM-pass polarizer, the minimum total polarization extinction ratio and insertion loss are $\text{PER}_{\text{Total}}^{\text{Polarizer}} = 164 \text{ dB/mm}$, $\text{IL}_{\text{Total}}^{\text{Polarizer}} = 3.86 \text{ dB/mm}$. It is clear that if the length of the active region increases, both extinction ratio and insertion losses will increase. The comparison of these results with the state-of-the-art of in-line fiber modulators/polarizers is shown in Table 1. Here, λ_{opr} denotes the operating wavelength.

Table 1: Comparison of the most significant related work.

Reference	λ_{opr} (nm)	Applied materials & structure	ER (dB) modulator		PER (dB) polarizer		IL (dB)	Speed (Hz)	Type
			Exp.	Sim.	Exp.	Sim.			
Lee et al. [35]	1550	Graphene on SPF	10	NA	-	-	<1	<300	EA
Zhang et al. [33]	1550	Graphene/PVB on SPF	9	NA	-	-	<1	500 G	AlOpt
Chen et al. [38]	1550	Graphene-microfiber	7	NA	-	-	NA	100 k	AlOpt
Cheng et al. [46]	1260–1700	Graphene/hBN Sandwich with photonic crystal fiber	~42	NA	-	-	NA	100 M	EA
Xiao et al. [24]	1550	Graphene of SPF	NA	35.78	-	-	NA	2.67 M	EA
Bao et al. [25]	480–1650	Graphene on SPF	-	-	27	~23	5–15	-	Absr.
Li et al. [47]	1550	Graphene on SPF	-	-	27	NA	5	-	Absr.
Xuan et al. [48]	1570–1620	Photonic bandgap fiber	-	-	30	NA	5.5–7	-	Absr.
Zhang et al. [27]	1425–1600	Graphene/PVB on SPF	-	-	28–41	26–47	1–4.8	-	Absr.
He et al. [49]	1550	Graphene/hBN stack on silicon-core fiber	-	-	NA	169–250	~20	-	Absr.
Guan et al. [20]	1485–1610	Graphene on surface-core fiber	-	-	NA	~26	~1	-	Absr.
Current work	1550	PMMA/graphene/VO ₂ /graphene on SPF	-	165	-	164	2.3/3.86	125 M	EA/Absr.

Abbreviations & acronyms: Exp. = experiment, Sim. = simulation, NA = not available, – = not applicable, EA = electro-absorptive, Absr. = absorptive, AlOpt = all-optic.

4 Modulation speed calculation

Generally, there are two mechanisms that can limit the modulation bandwidth or equivalently the response time of our proposed device that are schematically shown in Figure 7a and b. The first limitation is the electrical time constant of the device, $\tau^{\text{RC}} = R_t \times C_t$ where C_t and R_t denote the total capacitance and total resistance of the structure, respectively. When the device is in the on-state ($V_{\text{bias}} < V_{\text{th}}$) with the insulating VO₂ layer, the structure can be modeled as a parallel plate capacitor in which VO₂ plays the role of a dielectric sandwiched between two graphene electrodes. Switching the modulator from the on- to off-state is performed by applying an external bias a bias voltage higher than the threshold voltage ($V_{\text{th}} \approx 0.7$ V). However, it takes several RC time constants for the capacitor voltage to reach V_{th} as shown in Figure 7c (the blue line).

In order to estimate the RC time constant, the total resistance, R_t and capacitance, C_t of the structure should be calculated. The total capacitance of the structure is the series combination of the oxide capacitance, $C_{\text{ox}} = \epsilon_0 \epsilon_{\text{VO}_2}^{\text{DC}} / d$ (per unit area) and quantum capacitance of graphene layers, C_Q (see Supplement 1, Section II). The oxide capacitance per unit area is obtained as $C_{\text{ox}} = 29.5 \text{ fF}/\mu\text{m}^2$ for VO₂ dielectric constant of $\epsilon_{\text{VO}_2}^{\text{DC}} = 36$ [50] and a thickness of $d = 10.8$ nm. The quantum capacitance per unit area is also calculated to be $C_Q = 243 \text{ fF}/\mu\text{m}^2$, which is clearly much larger than the oxide capacitance. Consequently, the oxide capacitance is dominant in our proposed structure and the effect of the quantum capacitance can be ignored.

The total resistance of the device is the series combination of two Ti-Au/graphene contact resistances, R_c and two graphene sheet resistances, R_{sh} . Assuming a contact resistance of $200 \Omega \cdot \text{m}$ [51, 52], and a sheet resistance of $500 \Omega/\square$ (although a lower sheet resistance of about $120\text{--}280 \Omega/\square$ is achievable for a moderate doping level of $5 \times 10^{12} \text{ cm}^{-2}$ [53–55]), the RC time constant of about 1.18 ns is expected. It should be noted that the voltage across the VO₂ layer reaches 63, 95 and 99% of the bias voltage after $1\tau^{\text{RC}}$, $3\tau^{\text{RC}}$, and $5\tau^{\text{RC}}$, respectively. Thus, the RC time delay of the device implicitly depends on the value of the applied bias voltage so that the higher bias voltage increases results in a shorter delay time. For instance, if a bias of 1.1 V is applied, the VO₂ voltage reaches the threshold value just after one RC time constant.

The second mechanism that restricts the modulation speed is the insulating-to-conducting phase transition (ICPT) (or inversely, the conducting-to-insulating phase

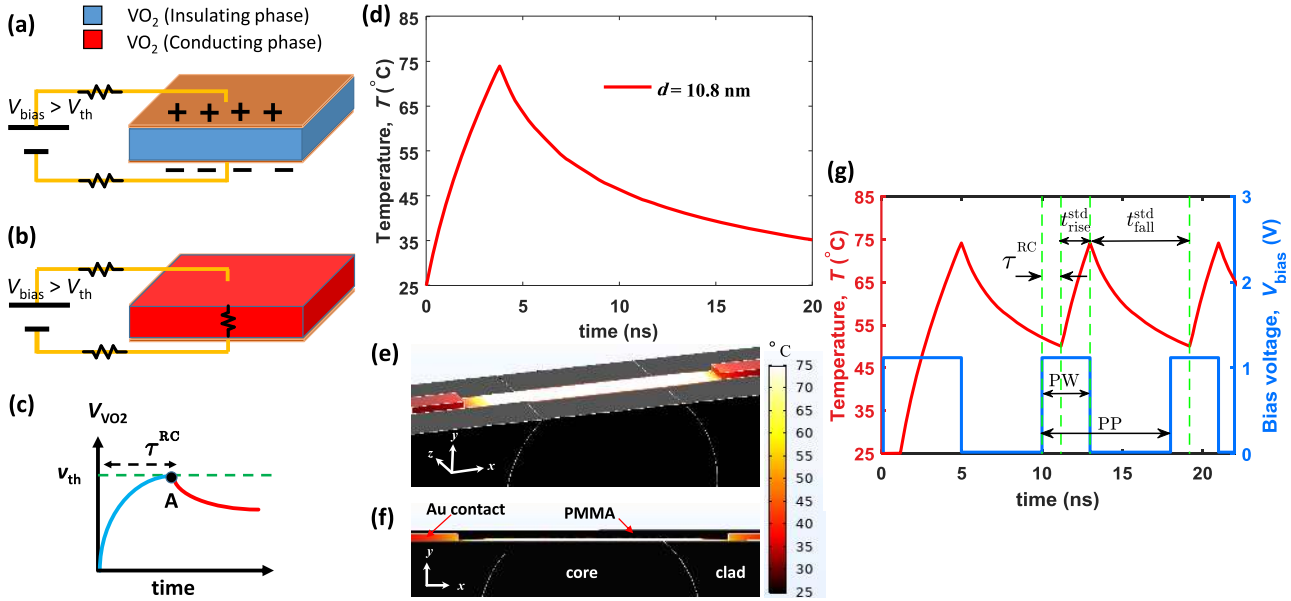


Figure 7: Modulation speed calculation. (a) The circuit model and phase-state of the device after applying the bias voltage before RC time delay of the device, i.e. $V_{VO_2} < V_{th}$, and (b) after RC time delay of the device, i.e. $V_{VO_2} \geq V_{th}$. (c) The voltage-time diagram of the voltage on the VO_2 layer after applying the bias voltage. (d) Temporal variation of the VO_2 temperature between 25°C and 75°C during ICPT and CIPT for $d = 10.8$ nm. (e) The 3D view of the spatial temperature distribution of the device at time $t = 4.2$ ns. Here, PMMA is made transparent so that the temperature distribution of VO_2 and Au contacts can be seen better. (f) 2D view of the device temperature distribution in the $x-y$ plane. (g) The steady-state operation of the TE modulator. The steady-state phase transition of VO_2 and hence the switching between the on- and off-states is induced by applying nanosecond electrical pulses with an amplitude 1.1 V, a width of $PW = 2.98$ ns, and a period of $PP = 8$ ns. The heating rise-time, $t_{rise}^{std} = 1.8$ ns and the cooling fall-time, $t_{fall}^{std} = 6.17$ ns and the time delay associated to the RC time constant of the device, $\tau^{RC} = 1.18$ ns are shown. In the steady-state operation the temperature of VO_2 varies between the lower limit and the upper limit of 50°C and 75°C, respectively.

transition (CIPT)) time of VO_2 . As discussed above, a proper external bias higher than the threshold voltage is applied to the graphene sheets during ICPT. Hence, charge carriers are injected into the VO_2 layer via the Poole-Frenkel mechanism [56], which results in rapid heating and resistivity reduction of VO_2 . Now, there is a current flow through the graphene/ VO_2 /graphene stack. As a result, the electric field drops and the temperature continues to rise by the electrical current and in this way, the thermal actuation of the device through Joule heating is accomplished (see the red line in Figure 7c).

When the phase of VO_2 changes from the insulating phase to the conducting phase, its resistivity significantly reduces by four orders of magnitude [57], resulting in a current flow through the VO_2 layer and graphene sheets which assist in further heating of the device. Figure 7d shows the temporal variation of temperature of the VO_2 layer in both ICPT and CIPT. The calculated heating time (ICPT) and cooling time (CIPT) for $d = 10.8$ nm is ~ 4.2 ns and ~ 16 ns, respectively. Note that the heating time is considered long enough (~ 4.2 ns) so that the VO_2 temperature rises above 68°C (up to ~ 75 °C) to ensure full ICPT. The 3D and 2D

view of the spatial temperature distribution of the device including the VO_2 layer, two graphene sheets and the SPF are presented in Figure 7e and f, respectively. The thermal simulation results shown in Figure 7d (temporal heat transfer) and Figure 7e and f (spatial temperature distribution) are obtained by solving the three-dimensional heat transfer equation by including both conduction and convection mechanisms. The heat conduction equation together with the electric current reads as [58, 59]:

$$\frac{\partial^2 T}{\partial x^2} + \frac{\partial^2 T}{\partial y^2} + \frac{\partial^2 T}{\partial z^2} + \frac{1}{k} g_{elec} = \frac{1}{\theta} \frac{\partial T}{\partial t} \quad (3)$$

where T , g_{elec} , k and $\theta = k/\rho C_p$ represent the temperature, heat generation, thermal conductivity and thermal diffusivity, respectively. Also, ρ is the material density, and C_p is the heat capacity. Here, the heat generation in the device is due to the electrical current flow through the VO_2 and two graphene sheets given by $g_{elec} = I^2 R_t$, where I and R_t denote the electric current and total resistance of the device, respectively (see Supplement 1, Section III and Figure S4). Equation (3) should be solved in each material separately, then the following boundary conditions must be applied at the interface of two materials in contact; (i)

$T_1 = T_2$ reveals that two materials in contact must have the same temperature at the interface, and (ii) $k_1 \nabla T_1 = k_2 \nabla T_2$ expresses the equality of heat conduction at the interface, where ∇ denotes the gradient operator (see Supplement 1, Section III and Figure S5(a)). It should be noted that the graphene, thanks to the highest thermal conductivity (up to $5300 \text{ W/m}^{-1} \text{ K}^{-1}$) [68, 69] among the known materials, provides the highest heat transfer capability and hence is a promising candidate to implement thermo-optic devices. Details of the thermal properties of the device materials at $\lambda = 1.55 \text{ }\mu\text{m}$ are given in Table 2.

As mentioned earlier, the convection mechanism must also be considered to account for the impact of the surrounding ambient, which includes a fluid such as air or water (that can be used as a coolant). The convection boundary condition must be applied to all the external boundaries of the device that are in contact with the ambient, as [58]:

$$q_{\text{conv}} = \gamma(T_{\text{intfc}} - T_{\text{amb}}), \quad \text{W/m}^2 \quad (4)$$

where q_{conv} is heat loss from the external interface at temperature T_{intfc} by convection mechanism into the ambient with the temperature $T_{\text{amb}} = 25^\circ\text{C}$ and the heat transfer coefficient of γ (see Supplement 1, Figure S5b).

Figure 7g shows the steady-state operation of the modulator by considering two mechanisms limiting the modulation rate, RC time constants, and heat transfer phenomena. As shown, we choose the temperature upper and lower limits of 75°C and of 50°C , respectively. These choices are due to the fact that the insulating to conducting phase transitions in VO_2 occurs at above 68°C and below 55°C , respectively, therefore it is enough to set the VO_2 temperature above 68°C and below 55°C . Here, to insure full phase transitions, the temperatures of 75°C and 50°C are chosen for steady-state operation. For insulating to conducting phase transition from the initial temperature of 50°C , a bias voltage with a pulse width (PW) of $\text{PW} = \tau^{\text{RC}} + t_{\text{rise}}^{\text{std}} = 2.98 \text{ ns}$, a pulse period (PP) of $\sim 8 \text{ ns}$, and an amplitude of 1.1 V are required. As can be seen, the bias pulse is set to be advanced by an amount of $\tau^{\text{RC}} = 1.18 \text{ ns}$, because the VO_2 voltage is always lagging the bias voltage and its take a time by the amount of RC time constant of τ^{RC} to bring the VO_2 voltage to the threshold voltage of 0.7 V . Then, the electrical current flows for a period of $t_{\text{rise}}^{\text{std}} = 1.8 \text{ ns}$, which raises the VO_2 temperature from 50°C to 75°C . On the other hand, to change the VO_2 phase from the conducting phase to the insulating phase, the electric current is turned off for a period of $t_{\text{fall}}^{\text{std}} = 6.17 \text{ ns}$ to allow heat dissipation during the cooling process. The steady-state results shown in Figure 7g reveal that a

Table 2: Optical and thermal properties of materials.

Material	Refractive index	Thermal conductivity k (W/m K)	Heat capacity C_p (J/kg K)	Density ρ (kg/m ³)
VO_2 (insulating) [16, 17, 60, 61]	$3.243 + 0.353i$	3.5	656	4571
VO_2 (conducting) [16, 17, 60, 61]	$1.58 + 2.63i$	5.5	757	4653
PMMA [63–65]	1.49	0.17	1260	1190
Au [65, 66]	$0.524 + 10.742i$	314	129	193,00
Silica (core & clad) [66, 67]	$1.4682 + 1.4615i$	1.38	703	2203
Graphene [4]	–	3000	2082	2267

modulation speed of $1/\text{PP} \approx 125$ MHz can be achieved. The comparison of the steady-state modulation speed of modulators is shown in Table 1. A comparison of the steady-state modulation velocities of the modulators is shown in Table 1. Moreover, the modulation energy consumption of the TE modulator can be obtained by [70]:

$$\text{Energy/bit} = \frac{1}{2} C_t V_{\text{bias}}^2 + \frac{V_{\text{bias}}^2}{R_t \times \text{BW}} \quad (5)$$

where the first term on the right hand side accounts for the capacitive loss across the VO_2 layer, the second term represents the Joule heating loss due to current flow and BW denotes the modulation bandwidth. Equation (5) yields a moderate Energy/bit of ~ 0.98547 pJ/bit.

5 Conclusions

In summary, an in-line VO_2 -based TE-modulator and TM-pass polarizer was proposed using an engineered stack of PMMA/graphene/ VO_2 /graphene on a side-polished fiber. The proposed design exhibits the capability of selective mode reshaping for different polarizations which could open several functionalities in integrated optical devices. This capability is applied to propose an ultra-high performance TE modulator/TM-pass polarizer in which the propagation loss of the desired polarization undergoes substantial changes upon the VO_2 phase transitions from the insulating to the conducting phase and vice versa. The VO_2 phase transitions that are governed by electric heating and heat dissipation are calculated by solving the transient heat transfer equations in three-dimensional space. According to the calculations, the VO_2 phase transition time for ICPT and CIPT in the steady-state operation is about 1.8 and 6.17 ns, respectively. Optical simulations are also performed based on the 3D-FDTD method. According to the simulation results, an ER of as high as 165 dB/mm and a low IL of only 2.3 dB/mm are obtained for the TE-modulator. In the case of the TM-pass polarizer, a PER of about 164 dB/mm with an IL of less than 3.86 dB/mm is achieved which is one order of magnitude larger than that in the previously studied polarizers. The TE modulator exhibits a high modulation speed of ~ 125 MHz. Moreover, the required bias voltage of the proposed modulator is as low as 1.1 V. The results demonstrate that active mode-reshaping is a promising approach for enhancing polarization-dependency of in-line optical devices.

Supplementary information

See Supplement 1 for supporting content.

Acknowledgment: M. Heidari thanks Dr. Mohammad Safarzadeh and Dr. Mohammad-Hossein Pourghasemian from the Department of Mechanical Engineering, Tarbiat Modares University for their help and fruitful discussions.

Author contribution: All the authors have accepted equal responsibility for the entire content of this submitted manuscript and approved submission.

Research funding: The authors received no specific funding for this work.

Conflict of interest statement: The authors declare no conflicts of interest regarding this article.

References

- [1] L. Mastronardi, M. Banakar, A. Khokhar, et al., "High-speed Si/GeSi hetero-structure electro absorption modulator," *Opt. Express*, vol. 26, pp. 6663–6673, 2018.
- [2] K. Liu, C. R. Ye, S. Khan, and V. J. Sorger, "Review and perspective on ultrafast wavelength-size electro-optic modulators," *Laser Photon. Rev.*, vol. 9, pp. 172–194, 2015.
- [3] W. E. Ross, D. Psaltis, and R. H. Anderson, "Two-dimensional magneto-optic spatial light modulator for signal processing," *Real-Time Signal Proc. V*, pp. 191–198, 1982.
- [4] J. T. Kim, K. H. Chung, and C.-G. Choi, "Thermo-optic mode extinction modulator based on graphene plasmonic waveguide," *Opt. Express*, vol. 21, pp. 15280–15286, 2013.
- [5] B. Janjan, M. Miri, D. Fathi, M. Heidari, and D. Abbott, "Modulator thermally triggered by a graphene microheater," *IEEE J. Sel. Top. Quant. Electron.*, vol. 26, p. 3400206, 2020.
- [6] M. Sadeghi, B. Janjan, M. Heidari, and D. Abbott, "Mid-infrared hybrid Si/ VO_2 modulator electrically driven by graphene electrodes," *Opt. Express*, vol. 28, pp. 9198–9207, 2020.
- [7] E. Mao, C. W. Coldren, J. S. Harris, D. R. Yankelevich, O. Solgaard, and A. Knoesen, "GaAs/AlGaAs multiple-quantum-well in-line fiber intensity modulator," *Appl. Phys. Lett.*, vol. 75, pp. 310–312, 1999.
- [8] Q. Gao, E. Li, and A. X. Wang, "Ultra-compact and broadband electro-absorption modulator using an epsilon-near-zero conductive oxide," *Photon. Res.*, vol. 6, pp. 277–281, 2018.
- [9] S. Vatani, H. Taleb, and M. K. Moravvej-Farshi, "Optical modulation via guided-mode resonance in an ITO-loaded distributed Bragg reflector topped with a two-dimensional grating," *IEEE J. Sel. Top. Quant. Electron.*, vol. 27, p. 3300307, 2021.
- [10] K. J. Miller, R. F. Haglund, and S. M. Weiss, "Optical phase change materials in integrated silicon photonic devices: review," *Opt. Mater. Express*, vol. 8, pp. 2415–2429, 2018.
- [11] M. Singh, S. K. Raghuwanshi, and T. Srinivas, "Nanophotonic on-chip hybrid plasmonic electro-optic modulator with phase change materials," *Phys. Lett.*, vol. 383, pp. 3196–3199, 2019.
- [12] X. Hu and J. Wang, "Design of graphene-based polarization-insensitive optical modulator," *Nanophotonics*, vol. 7, pp. 651–658, 2018.

- [13] C. Wan, E. H. Horak, J. King, et al., “Limiting optical diodes enabled by the phase transition of vanadium dioxide,” *ACS Photonics*, vol. 5, pp. 2688–2692, 2018.
- [14] S. Zhang, M. A. Kats, Y. Cui, et al., “Current-modulated optical properties of vanadium dioxide thin films in the phase transition region,” *Appl. Phys. Lett.*, vol. 105, p. 211104, 2014.
- [15] B. Wu, A. Zimmers, H. Aubin, R. Ghosh, Y. Liu, and R. Lopez, “Electric-field-driven phase transition in vanadium dioxide,” *Phys. Rev. B*, vol. 84, p. 241410, 2011.
- [16] C. Wan, Z. Zhang, D. Woolf, et al., “On the optical properties of thin-film vanadium dioxide from the visible to the far infrared,” *Ann. Phys.*, vol. 531, p. 1900188, 2019.
- [17] M. Currie, M. A. Mastro, and V. D. Wheeler, “Characterizing the tunable refractive index of vanadium dioxide,” *Opt. Mater. Express*, vol. 7, pp. 1697–1707, 2017.
- [18] B. Janjan, M. Miri, A. Zarifkar, and M. Heidari, “Design and simulation of compact optical modulators and switches based on Si–VO₂–Si horizontal slot waveguides,” *J. Lightwave Technol.*, vol. 35, pp. 3020–3028, 2017.
- [19] S. Mohammadi-Pouyan, M. Miri, and M. H. Sheikhi, “Design of a vanadium dioxide-based dual-polarization optical PAM4 modulator,” *J. Opt. Soc. Am. B*, vol. 35, pp. 3094–3103, 2018.
- [20] C. Guan, S. Li, Y. Shen, T. Yuan, J. Yang, and L. Yuan, “Graphene-Coated surface core fiber polarizer,” *J. Lightwave Technol.*, vol. 33, pp. 349–353, 2015.
- [21] J. Dong, Y. Zhang, Y. Wang, et al., “Side-polished few-mode fiber based surface plasmon resonance biosensor,” *Opt. Express*, vol. 27, pp. 11348–11360, 2019.
- [22] S.-M. Tseng and C.-L. Chen, “Side-polished fibers,” *Appl. Opt.*, vol. 31, pp. 3438–3447, 1992.
- [23] D. G. Moodie and W. Johnstone, “Wavelength tunability of components based on the evanescent coupling from a side-polished fiber to a high-index-overlay waveguide,” *Opt. Lett.*, vol. 18, pp. 1025–1027, 1993.
- [24] Y. Xiao, J. Zhang, J. Yu, et al., “Theoretical investigation of optical modulators based on graphene-coated side-polished fiber,” *Opt. Express*, vol. 26, pp. 13759–13772, 2018.
- [25] Q. Bao, H. Zhang, B. Wang, et al., “Broadband graphene polarizer,” *Nat. Photonics*, vol. 5, pp. 411–415, 2011.
- [26] R. B. Dyott, J. Bello, and V. A. Handerek, “Indium-coated D-shaped-fiber polarizer,” *Opt. Lett.*, vol. 12, pp. 287–289, 1987.
- [27] H. Zhang, N. Healy, L. Shen, et al., “Graphene-based fiber polarizer with PVB-enhanced light interaction,” *J. Lightwave Technol.*, vol. 34, pp. 3563–3567, 2016.
- [28] J. Yu, S. Jin, Q. Wei, et al., “Hybrid optical fiber add-drop filter based on wavelength dependent light coupling between micro/nano fiber ring and side-polished fiber,” *Sci. Rep.*, vol. 5, p. 7710, 2015.
- [29] R. Chu, C. Guan, Y. Bo, et al., “All-optical graphene-oxide humidity sensor based on a side-polished symmetrical twin-core fiber Michelson interferometer,” *Sensor. Actuator. B Chem.*, vol. 284, pp. 623–627, 2019.
- [30] X. Yang, S. Bandyopadhyay, L. Shao, D. Xiao, G. Gu, and Z. Song, “Side-polished DBR fiber laser with enhanced sensitivity for axial force and refractive index measurement,” *IEEE Photonics J.*, vol. 11, p. 7101910, 2019.
- [31] H. S. Jang, K. N. Park, J. P. Kim, et al., “Sensitive DNA biosensor based on a long-period grating formed on the side-polished fiber surface,” *Opt. Express*, vol. 17, pp. 3855–3860, 2009.
- [32] N.-K. Chen, S. Chi, and S.-M. Tseng, “Wideband tunable fiber short-pass filter based on side-polished fiber with dispersive polymer overlay,” *Opt. Lett.*, vol. 29, pp. 2219–2221, 2004.
- [33] H. Zhang, N. Healy, L. Shen, C. C. Huang, D. W. Hewak, and A. C. Peacock, “Enhanced all-optical modulation in a graphene-coated fibre with low insertion loss,” *Sci. Rep.*, vol. 6, p. 23512, 2016.
- [34] H. Nikbakht, H. Latifi, G.-M. Parsanasab, M. Taghavi, and M. Riyahi, “Utilizing polarization-selective mode shaping by chalcogenide thin film to enhance the performance of graphene-based integrated optical devices,” *Sci. Rep.*, vol. 9, p. 12446, 2019.
- [35] E. J. Lee, S. Y. Choi, J. Hwanseong, et al., “Active control of all-fibre graphene devices with electrical gating,” *Nat. Commun.*, vol. 6, p. 6851, 2015.
- [36] M. Heidari and V. Ahmadi, “Graphene-based mid-infrared plasmonic isolator with multimode interferometer,” *Opt. Lett.*, vol. 45, pp. 5764–5767, 2020.
- [37] M. Karimi, V. Ahmadi, and M. Ghezelsefloo, “Graphene-based side-polished optical fiber amplifier,” *Appl. Opt.*, vol. 55, pp. 10417–10422, 2016.
- [38] J. H. Chen, B. C. Zheng, G. H. Shao, S. J. Ge, F. Xu, and Y. Q. Lu, “An all-optical modulator based on a stereo graphene-microfiber structure,” *Light Sci. Appl.*, vol. 4, no. 12, p. e360, 2015.
- [39] M. Heidari and V. Ahmadi, “Design and analysis of a graphene magneto-plasmon waveguide for plasmonic mode switch,” *IEEE Access*, vol. 7, pp. 43406–43413, 2019.
- [40] Y. Guo, X. Sun, J. Jiang, et al., “A reconfigurable remotely epitaxial VO₂ electrical heterostructure,” *Nano Lett.*, vol. 20, pp. 33–42, 2020.
- [41] M. M. Fadlilmula, E. C. Sürmeli, M. Ramezani, and T. S. Kasirga, “Effects of thickness on the metal–insulator transition in free-standing vanadium dioxide nanocrystals,” *Nano Lett.*, vol. 17, pp. 1762–1767, 2017.
- [42] K. Han, L. Wu, Y. Cao, et al., “Enhanced metal–insulator transition in freestanding VO₂ down to 5 nm thickness,” *ACS Appl. Mater. Interfaces*, vol. 13, pp. 16688–16693, 2021.
- [43] K. Martens, N. Aetukuri, J. Jeong, M. G. Samant, and S. S. P. Parkin, “Improved metal-insulator-transition characteristics of ultrathin VO₂ epitaxial films by optimized surface preparation of rutile TiO₂ substrates,” *Appl. Phys. Lett.*, vol. 104, p. 081918, 2014.
- [44] A. P. Peter, K. Martens, G. Rampelberg, et al., “Metal-Insulator transition in ALD VO₂ ultrathin films and nanoparticles: morphological control,” *Adv. Funct. Mater.*, vol. 25, pp. 679–686, 2015.
- [45] H. Dong, L. Chen, J. Zhou, et al., “Coreless side-polished fiber: a novel fiber structure for multimode interference and highly sensitive refractive index sensors,” *Opt. Express*, vol. 25, pp. 5352–5365, 2017.
- [46] X. Cheng, X. Zhou, L. Tao, et al., “Sandwiched graphene/hBN/graphene photonic crystal fibers with high electro-optical modulation depth and speed,” *Nanoscale*, vol. 12, pp. 14472–14478, 2020.

- [47] W. Li, L. Yi, R. Zheng, Z. Ni, and W. Hu, "Fabrication and application of a graphene polarizer with strong saturable absorption," *Photon. Res.*, vol. 4, pp. 41–44, 2016.
- [48] H. F. Xuan, W. Jin, J. Ju, et al., "Hollow-core photonic bandgap fiber polarizer," *Opt. Lett.*, vol. 33, pp. 845–847, 2008.
- [49] X. He, A. Hu, and X. Guo, "In-fiber graphene-hBN polarizer with enhanced performance and bandwidth," *IEEE Photonics J.*, vol. 11, p. 7104608, 2019.
- [50] Z. Yang, C. Ko, V. Balakrishnan, G. Gopalakrishnan, and S. Ramanathan, "Dielectric and carrier transport properties of vanadium dioxide thin films across the phase transition utilizing gated capacitor devices," *Phys. Rev. B*, vol. 82, p. 205101, 2010.
- [51] F. Giubileo and A. Di Bartolomeo, "The role of contact resistance in graphene field-effect devices," *Prog. Surf. Sci.*, vol. 92, pp. 143–175, 2017.
- [52] S. M. Song, J. K. Park, O. J. Sul, and B. J. Cho, "Determination of work function of graphene under a metal electrode and its role in contact resistance," *Nano Lett.*, vol. 12, pp. 3887–3892, 2012.
- [53] G. V. Bianco, A. Sacchetti, A. Milella, et al., "Extraordinary low sheet resistance of CVD graphene by thionyl chloride chemical doping," *Carbon*, vol. 170, pp. 75–84, 2020.
- [54] S. Bae, H. Kim, Y. Lee, et al., "Roll-to-roll production of 30-inch graphene films for transparent electrodes," *Nat. Nanotechnol.*, vol. 5, pp. 574–578, 2010.
- [55] K. S. Kim, Y. Zhao, H. Jang, et al., "Large-scale pattern growth of graphene films for stretchable transparent electrodes," *Nature*, vol. 457, pp. 706–710, 2009.
- [56] P. Markov, R. E. Marvel, H. J. Conley, K. J. Miller, R. F. Haglund, and S. M. Weiss, "Optically monitored electrical switching in VO₂," *ACS Photonics*, vol. 2, pp. 1175–1182, 2015.
- [57] Z. Shao, X. Cao, H. Luo, and P. Jin, "Recent progress in the phase-transition mechanism and modulation of vanadium dioxide materials," *NPG Asia Mater.*, vol. 10, pp. 581–605, 2018.
- [58] M. N. Özışık, *Heat Conduction*, 2nd ed. New York, John Wiley & Sons, 1993.
- [59] B. Zalba, J. M. Marin, L. F. Cabeza, and H. Mehling, "Review on thermal energy storage with phase change: materials, heat transfer analysis and applications," *Appl. Therm. Eng.*, vol. 23, pp. 251–283, 2003.
- [60] D.-W. Oh, C. Ko, S. Ramanathan, and D. G. Cahill, "Thermal conductivity and dynamic heat capacity across the metal-insulator transition in thin film VO₂," *Appl. Phys. Lett.*, vol. 96, p. 151906, 2010.
- [61] G. Chandrashekhar, H. Barros, and J. Honig, "Heat capacity of VO₂ single crystals," *Mater. Res. Bull.*, vol. 8, pp. 369–374, 1973.
- [62] M. J. Assael, S. Botsios, K. Gialou, and I. N. Metaxa, "Thermal conductivity of polymethyl methacrylate (PMMA) and borosilicate crown glass BK7," *Int. J. Thermophys.*, vol. 26, pp. 1595–1605, 2005.
- [63] A. Soldera, N. Metatla, A. Beaudoin, S. Said, and Y. Grohens, "Heat capacities of both PMMA stereomers: comparison between atomistic simulation and experimental data," *Polymer*, vol. 51, pp. 2106–2111, 2010.
- [64] M. Piliarik, P. Kvasnička, N. Galler, J. R. Krenn, and J. Homola, "Local refractive index sensitivity of plasmonic nanoparticles," *Opt. Express*, vol. 19, pp. 9213–9220, 2011.
- [65] Y. Takahashi and H. Akiyama, "Heat capacity of gold from 80 to 1000 K," *Thermochim. Acta*, vol. 109, pp. 105–109, 1986.
- [66] E. D. Palik, *Handbook of Optical Constants of Solids*, vol. 3, San Diego, Academic Press, 1998.
- [67] J. A. Malen, K. Baheti, T. Tong, Y. Zhao, J. A. Hudgings, and A. Majumdar, "Optical measurement of thermal conductivity using fiber aligned frequency domain thermoreflectance," *J. Heat Tran.*, vol. 133, 2011. <https://doi.org/10.1115/1.4003545>.
- [68] A. A. Balandin, S. Ghosh, W. Bao, et al., "Superior thermal conductivity of single-layer graphene," *Nano Lett.*, vol. 8, pp. 902–907, 2008.
- [69] S. Ghosh, I. Calizo, D. Teweldebrhan, et al., "Extremely high thermal conductivity of graphene: prospects for thermal management applications in nanoelectronic circuits," *Appl. Phys. Lett.*, vol. 92, p. 151911, 2008.
- [70] K. J. Ooi, P. Bai, H. S. Chu, and L. K. Ang, "Ultracompact vanadium dioxide dual-mode plasmonic waveguide electroabsorption modulator," *Nanophotonics*, vol. 2, pp. 13–19, 2013.

Supplementary Material: The online version of this article offers supplementary material (<https://doi.org/10.1515/nanoph-2021-0225>).